scientific reports

Check for updates

OPEN

Thermoresponsive NDP hydrogel embedded with MnO_2 nanoparticles for postoperative antirecurrence therapy in pancreatic cancer

Zhongxu Yuan[1,2], Shuai Ma[3], Liang Yan[2], Man Xu[2], Dongquan Liu[2], Weicheng Wang[2], Bowen Han[2], Gan Chen[2] & Zhengguang Wang[1]✉

Surgical resection remains a potentially curative treatment option for pancreatic cancer (PC). However, the high rate of local tumor recurrence and poor prognosis severely limit its therapeutic efficacy. In this study, we report an injectable thermosensitive hydrogel platform (designated as NDP@MnO_2 hydrogel) that exhibits excellent biocompatibility, photothermal performance, and wet adhesion properties, specifically designed for precise post-operative therapy. This thermosensitive system innovatively combines shear-thinning injectability, dopamine-mediated tissue adhesion, and MnO_2-enhanced photothermal ablation capabilities. By precisely targeting hyperthermia to the moist and irregular pancreatic resection margins during the sol-gel transition and subsequent exposure to an 808 nm laser, this approach can effectively and selectively eliminate residual tumor cells while minimizing collateral damage to adjacent healthy tissues. Notably, pre-clinical studies have demonstrated that this approach significantly reduces the locoregional recurrence rate in pancreatic cancer models, thereby offering a promising solution to the critical issue of postoperative recurrence.

Keywords Hydrogel, Photothermal therapy, Pancreatic cancer, Postoperative recurrence

Pancreatic cancer (PC) is well-known for its extreme malignancy and high mortality, having a five-year survival rate of less than 12%[1,2]. Surgical resection is the preferred treatment for resectable PC patients[3]. However, the efficacy of surgery is significantly undermined by the high local recurrence rate of 20–50% following tumor resection, which is due to the invasive nature of PC cells[4]. Furthermore, the complex anatomical structure surrounding the pancreas renders complete resection difficult[5]. Since the tumor is encircled by a complex network of blood vessels and nerves, it is hard to ensure that there is no residual tumor tissue after resection[6]. Therefore, effectively removing residual tumor tissue to lower recurrence rates remains a significant challenge in the treatment of PC[7–10].

Numerous strategies, including intraoperative radiotherapy and the implantation of chemotherapeutic agents or radioactive particles, have been investigated to decrease tumor residues and reduce the risk of local recurrence[11–13]. Nevertheless, the distinctive pathobiological characteristics of PC, such as a dense desmoplastic stroma and poor vascularity, make most non-surgical treatment options largely be limited[14]. The systemic toxicity caused by radiotherapy and chemotherapy is also a crucial factor leading to the worsening of postoperative prognosis[15–17].

Manganese dioxide (MnO_2) nanoparticles have become a multifunctional anti-cancer agent and are frequently utilized as a photothermal agent in photothermal therapy (PTT)[18–20]. MnO_2 can act as an oxygen carrier in anti-cancer treatment, catalyzing the release of hydrogen peroxide in the tumor micro environment (TME) to relieve its hypoxic and acidic states[21]. In addition, MnO_2 interacts with the antioxidant glutathione (GSH) in the TME, decreasing the consumption of singlet oxygen generated during PTT and markedly enhancing its

[1]Department of General Surgery, The First Affiliated Hospital of Anhui Medical University, No. 218 Jixi Road, Shushan District, Hefei 230022, Anhui, China. [2]Department of General Surgery, Anhui No. 2 Provincial People's Hospital, No. 1868 Dangshan and North Second Ring Road, Yaohai District, Hefei 230041, Anhui, China. [3]Graduate School, Bengbu Medical University, No. 2600 Donghai Road, Longzihu District, Bengbu 233030, Anhui, China. ✉email: wangzhengguang@ahmu.edu.cn

effectiveness[22,23]. However, although MnO_2 nanoparticles have the potential to modulate tumor hypoxia and enhance photothermal therapy, systemic delivery through the venous system often fails to reach therapeutic intratumoral concentrations because of the hypovascular and desmoplastic characteristics of pancreatic tumors. To overcome this limitation, our strategy utilizes intraoperative hydrogel deposition to enable local retention of MnO_2 at resection sites for continuous TME modulation[24–26].

Recently, hydrogels have emerged as a promising platform for local combination therapies due to their biocompatibility, adjustable physicochemical properties, controllable structure, and easy functionalization[27]. However, traditional hydrogels face significant challenges in adhering to slippery wounds, which not only hinders the long-term retention of photothermal agents but also poses a major obstacle for practical applications, as most hydrogel studies have focused on surface wounds and neglected the moist and irregular environment characteristic of postoperative pancreatic cancer wounds[28,29]. To address these issues, hydrogels need to meet new requirements, such as effectively and firmly adhering to pancreatic wounds. Moreover, the irregular shape of postoperative pancreatic cancer wounds requires hydrogels to have excellent conformal properties to ensure accurate wound closure. Traditional prefabricated hydrogels are limited by their fixed morphology, and this restricts their ability to meet these stringent requirements[30].

In this research, we report the development of an injectable thermo-responsive hybrid hydrogel that exhibits strong wet tissue adhesion and conforms to irregular and uneven wound surfaces. This hydrogel serves as a delivery platform for MnO_2 nanoparticles in the photothermal treatment of postoperative pancreatic cancer wounds. PEG-modified MnO_2 nanoparticles (referred to as MnO_2-PEG NPs) were incorporated into the pre-synthesized poly((N-isopropyl acrylamide-co-dopamine)-b-poly(ethylene glycol)-b-poly(N-isopropyl acrylamide-co-dopamine)) ((NIPAM-co-NSA)-poly(ethylene glycol)-(NIPAM-co-NSA)) (abbreviated as NDP@MnO_2 or NDP-MnO_2 (NGM)) matrix to prepare the thermo-responsive hydrogel (Fig. 1a). The NDP@MnO_2 can be injected into the postoperative pancreatic wound via clinical needles in solution form and subsequently transforms into a stable gel state upon exposure to body temperature (Fig. 1b). Remarkably, the NDP@MnO_2 hydrogel demonstrates excellent adhesion to moist postoperative wounds. During the sol-gel transition, it leverages its excellent fluidity and permeability to fully fill and accurately seal irregular wound surfaces. When combined with photothermal therapy, this method effectively eliminates residual tumor cells, thus reducing the risk of postoperative recurrence. This approach based on novel hydrogel holds significant promise for improving the prognosis of pancreatic cancer patients and may potentially revolutionize the current postoperative treatment paradigm.

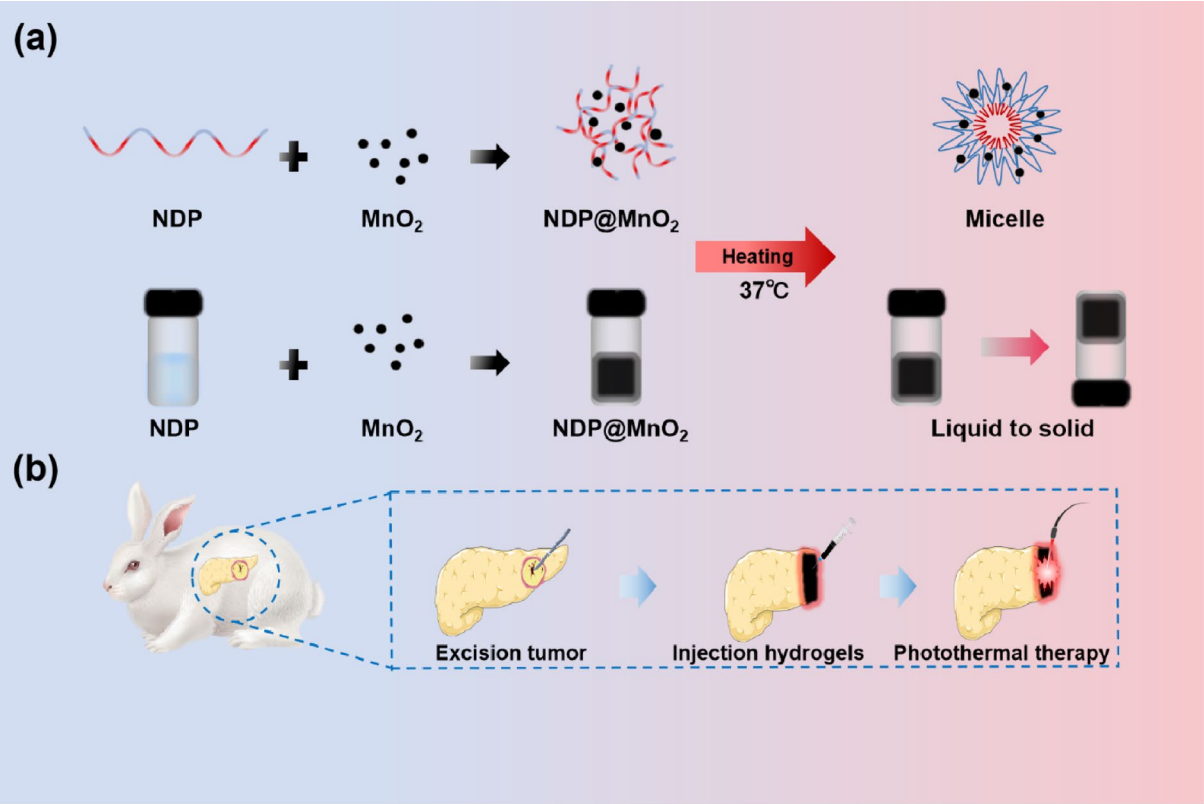

Fig. 1. Schematic diagram of hydrogel synthesis and treatment for pancreatic cancer. (**a**) Hybrid hydrogels were prepared by incorporating NDP and MnO_2 into a pre-gel water suspension, which rapidly transitions to a solid gel upon exposure to physiological temperature (37 ℃). (**b**) The hydrogel suspension was injected into the resection site in an animal model following pancreatic tumor resection, followed by photothermal therapy using an 808 nm laser.

Materials and methods

Materials

Unless otherwise specified, all chemicals were procured from Aldrich and utilized in accordance with the manufacturer's guidelines. Any special reagents or materials will be highlighted.

Cells and animals

The Panc-02 mouse pancreatic carcinoma cell line and the necessary biological reagents were obtained from Wuhan Servicebio. These cells were maintained in RPMI-1640 medium supplemented with 10% fetal bovine serum (FBS) and supplemented with 100 U/mL penicillin-streptomycin. The cultures were incubated at 37 ℃ in a humidified environment with 5% CO_2. Once adherent cells reached over 80% confluence, they were dissociated using 0.25% trypsin and subsequently passaged to promote further proliferation. A total of sixty 7-week-old female C57BL/6J mice were purchased from Henan Skbex Biology, while nine 3-month-old male New Zealand rabbits were sourced from Pizhou Dongfang. All animals were housed in a specific pathogen-free (SPF) facility, which was maintained at a constant temperature of 24 ± 2 ℃ with a 12-hour light-dark cycle. They had ad libitum access to food and water. Following anesthesia with 1% isoflurane, both the mice and rabbits were used for subsequent experimental procedures. The rabbits were humanely euthanized via intravenous air embolism, and the mice were sacrificed through cervical dislocation. All animal experiments complied with to protocols approved by the Institutional Animal Care and Use Committee (IACUC) of Hefei University of Technology.

Hydrogel preparation

To synthesize poly ((N-isopropylacrylamid-co-N-succinimidyl acrylate)-b-poly (ethylene glycol)-b-poly (N-isopropylacrylamide-co-N-succinimidyl acrylate)) (abbreviated as poly (NIPAM-co-NSA)-PEG-poly (NIPAM-co-NSA) or NDP), the following procedure was employed.

First, N-isopropylacrylamide (NIPAM, 0.996 g, 8.8 mmol), N-Succinimidyl Acrylate (NSA, 0.186 g, 1.1 mmol), AIBN (0.0018 g, 0.011 mmol), and CTA-PEG-CTA (0.1 g, 0.022 mmol) were dissolved in 3 mL of dioxane. The reaction mixture was underwent three freeze-pump-thaw cycles under nitrogen to remove dissolved oxygen. Subsequently, the reaction mixture was stirred at 78 °C for 24 h. After the reaction, the product was precipitated three times with ethyl ether and dried under vacuum overnight. This process resulted in 0.83 g of poly (NIPAM-co-NSA)-poly (ethylene glycol)-poly (NIPAM-co-NSA) as a white solid, with a yield of 90.1%. The polymer solutions were stored at 4 °C before further experiments and characterizations.

The NDP@MnO_2 hydrogel was prepared as follows. MnO_2 nanoparticles (100 nm, obtained from Shanghai Macklin) were pre-functionalized with dopamine via π-π stacking interactions to enhance interfacial compatibility. Then, the modified nanoparticles were added to a 15 wt% NDP copolymer solution, and the mixture was homogenized by probe sonication at 20 kHz frequency and 30% amplitude for 5 min. This process ensured the uniform distribution of MnO_2 nanoparticles within the hydrogel matrix.

Mechanical performance of hybrid hydrogels

Before performing uniaxial tensile measurements, the ambient temperature was adjusted to 37 °C to ensure that the hydrogel maintained its structural integrity. Specifically, NDP@MnO_2 hydrogel samples containing 2 wt% MnO_2 were prepared by cutting them into rectangular specimens measuring $20 \times 6 \times 0.3$ cm^3 for the test. These specimens were subjected to tensile loading at a rate of 20 mm/min until failure, and this procedure was repeated three times to ensure data reliability and consistency.

In vitro adhesive strength test of the hydrogel

To evaluate the mechanical stability and fatigue resistance of the solidified hydrogel under load, a series of stress-strain tests were conducted. Two pieces of porcine skin were adhered together with the hydrogel, and a weight was hung on one end. The weight was gradually increased until the bond broken. The maximum load at failure was recorded. Subsequently, the porcine skin glued by the gel were fixed in the Digital Tensile Tester to record the stress values during gel stretching. The adhesive ability of the hydrogel in wet environments was observed. The hydrogel was injected onto the surface of rabbit pancreatic tissue. After solidification, the tissue was immersed in deionized water and stirred for 5 min. The adhesion status of the hydrogel on the pancreatic tissue was then observed and recorded to determine whether it remained intact.

In vitro temperature-sensitive properties

The hydrogel was heated in a water bath until it transitioned from a liquid to a gel state. The temperature at which solidification occurred was recorded.

In vitro heating properties

NDP, MnO_2, and NDP@MnO_2 were respectively added to EP tubes. The tubes were irradiated with an 808 nm near-infrared (NIR) laser, and the resulting temperature changes were recorded using an Infrared thermal imager (Fluke ti400U). In vitro warming profiles and thermal efficiency were generated with Origin software.

In vitro evaluation of cell cytotoxicity

To evaluate the cytotoxic effect of the hydrogel on pancreatic cancer cells, a concentration gradient of dilutions was prepared. The hydrogel was diluted to concentrations of 25, 50, 100, and 200 mg/mL. Panc-02 cells in the logarithmic growth phase were seeded into plates, and the prepared solutions were added accordingly. After 24 h of incubation, the cells were treated with CCK-8 reagent, and the absorbance (OD) values were measured using a microplate reader. To assess the combined photothermal therapy effect on pancreatic cancer cells, undiluted hydrogel was added to the cell plates, followed by irradiation with an 808 nm near-infrared (NIR) laser for

5 min. Cell viability was subsequently evaluated using the CCK-8 reagent. Additionally, cells were stained with Calcein AM/PI fluorescent working solution and observed under a fluorescence microscope, where live cells appeared green and dead cells appeared red. The cell survival rate was calculated using the formula: [(As - Ab)/(Ac - Ab)]×100%, where As is the absorbance of the experimental well, Ac is the absorbance of the control well, and Ab is the absorbance of the blank well.

In vivo tumor models and treatment

To verify the efficacy of hydrogel combined with PTT in preventing recurrence after local tumor resection. We chose the C57BL/6J mouse subcutaneous tumor model as the research object. All mice were adapted for at least 3 days before the experiment. Firstly, the hair on the right thigh of mice ($n = 30$, 7 W) will be removed. Then the mice were subcutaneously injected with mouse pancreatic ductal carcinoma cells (Panc-02) (0.1 ml×1 × 10^6 cells/ml). The modeling was completed when the tumor diameter reaches 5 mm. All mice will be randomly divided into three groups: PBS group, NDP@MnO_2 group, NDP@MnO_2 + PTT group. Three groups of mice underwent tumor resection under 1% isoflurane anesthesia. The PBS group did not receive any treatment after tumor resection. NDP@MnO_2 group was injected with hydrogel at the cutting edge after the tumor was removed. The NDP@MnO_2 + PTT group tumors were first removed. Then, the hydrogel was injected into the tumor margin to perform photothermal therapy (PTT). The infrared emitted by the 808 nm infrared NIR generator would be used for PTT, and the Fluke ti400U infrared thermometer would be used for temperature monitoring. The temperature in the photothermal region was maintained at 50 °C for 5 min. All grouped mice were injected with 100,000 units/ml penicillin 0.1 ml to prevent infection after the experiment. The mice were observed every two days after the experiment. The mice's body weight was measured and recorded changes in 16 days. The tumor sizes were measured every two days using a caliper and calculated using the following equation $V = L \times W^2/2$. The mice were euthanized through cervical dislocation 16 days later. Recurrent tumor specimens were obtained and subjected to hematoxylin and eosin (H&E) staining along with immunohistochemical analysis to evaluate histopathological characteristics and protein expression profiles.

To verify the efficacy of hydrogel combined with PTT in preventing recurrence of pancreatic tumor in situ after resection. We chose the rabbit pancreas in situ model as the research object. All rabbits were adapted for at least one week before use. Male New Zealand rabbits ($n = 9$, 90 days) were anesthetized with 1% isoflurane and their abdominal hair was shaved off. After anesthesia, the rabbit was subjected to open abdominal exploration. VX2 tumor tissue block was implanted into the 18 G puncture needle core and punctured into the pancreas. Following hemostasis, the wound was irrigated with sterile saline and closed using 3 – 0 absorbable sutures in the abdominal region. Mice received a subcutaneous injection of 2 mL penicillin at a concentration of 100,000 units/ml for infection prophylaxis. One week later, the modeling was completed when tumor enhancement appears around the pancreas on Computed Tomography (CT) scan. All rabbits will be randomly divided into three groups: PBS group, NDP@MnO_2 group, NDP@MnO_2 + PTT group. The experimental procedure was the same as the mouse experiment, and the recurrence rate was assessed by CT scan of the pancreas after 16 days. The rabbit has recovered from tumors after being euthanized to perform TUNEL and H&E staining.

Biosafety assays

The immortalized human hepatic epithelial cell line (THLE-2) and the human acute monocytic leukemia cell line (THP-1) were used to evaluate the cytotoxicity of the hydrogel. Following a 24-hour co-culture of THLE-2 and THP-1 cells with the hydrogel, the cells were stained with Calcein-AM/PI reagent to distinguish between live and dead cells. Fluorescence microscopy was used to capture cell fluorescence images, and ImageJ software was utilized for quantitative analysis of fluorescence intensity.

Hemolysis assays were conducted to evaluate whether NDP@MnO_2 induced erythrocyte lysis. Rabbit whole blood samples were collected and incubated with various materials (deionized water, physiological saline, NDP, MnO_2 and NDP@MnO_2) for 24 h. The optical density (OD) values at 541 nm of the supernatant samples obtained by centrifugation were measured using a microplate reader. The hemolysis rate was calculated using the formula: [(As - Ac)/At]×100%, where As represents the absorbance of the sample, Ac is the absorbance of the physiological saline solution, and At is the absorbance of the deionized water group. The in vivo biocompatibility of NDP@MnO_2 was further assessed through animal biosafety evaluations. C57BL/6J mice were divided into an experimental group and a control group. Physiological saline and NDP@MnO_2 were respectively injected subcutaneously into the right hind legs of the mice in each group. After 14 days, blood samples were collected to measure biochemical indicators, and the hearts, livers, spleens, lungs, and kidneys were harvested for H&E staining.

Statistical analysis

All data are presented as mean ± standard deviation. The one-way ANOVA and independent-sample t-test were employed to assess the statistical significance between groups. Statistical analyses were conducted using IBM SPSS Statistics 23, ImageJ, Origin 2022, SmartView IR, Case Viewer, and Adobe Illustrator 2024. A P-value < 0.05 was considered statistically significant ($^*P < 0.05$, $^{**}P < 0.01$, $^{***}P < 0.001$, $^{****}P < 0.0001$).

Results and discussion

Preparation of hybrid hydrogels

The triblock copolymer poly(N-isopropylacrylamide-co-dopa)-b-poly(N-isopropylacrylamide-co-dopa) (NDP) was synthesized via the reaction between 4-cyano-4-(phenylthiocarbonyl sulfide) valeric acid (CTA) and NH_2-PEG-NH_2. Subsequently, a hybrid hydrogel was fabricated using NDP as the base material. The detailed synthesis process of NDP is illustrated in Fig. 2a. The ^{1}H NMR spectrum of the macro-CTA, presented in Figure S1, indicates that peak a corresponds to the proton chemical shift of -CH_2- in NHS, while peak b represents

the proton chemical shift of -CH_3 in NIPAM. The presence of these distinct hydrogen proton peaks confirms the successful initiation of the polymerization reaction by CTA-PEG-CTA, resulting in the formation of the hydrogel polymer precursor NDP.

Manganese dioxide nanoparticles (MnO_2 NPs) exhibit excellent biocompatibility and photothermal properties, making them promising candidates for tumor diagnosis and treatment[31]. Previous studies have demonstrated that MnO_2 NPs irradiated with near-infrared (NIR) laser light display rapid photo-responsive behavior and high photothermal conversion efficiency, offering the potential for spatiotemporally controllable hyperthermia therapy in photothermal therapy (PTT)[32]. MnO_2 NPs have been considered a novel type of PTT photosensitizer[33]. An aqueous dispersion of 100 nm diameter ultrasonically fractured MnO_2 NPs was mixed with NDP to prepare the NDP@MnO_2 hydrogel. As shown in Fig. 2g, the dynamic light scattering (DLS) showed the size of MnO_2 nanoparticles particles is approximately 100 nm. As shown in the scanning electron microscope (SEM) images in Figs. 2b and S2, the size of NDP@MnO_2 particles is approximately 150 nm. SEM images of the freeze-dried NDP@MnO_2 hydrogel reveal its characteristic three-dimensional porous structure. Energy-dispersive X-ray spectroscopy (EDS) element mapping, as presented in Fig. 2d, further confirms the uniform distribution of nanoscale MnO_2 particles within the synthesized NDP@MnO_2 hydrogel. The corresponding X-ray diffraction (XRD) patterns depicted in Fig. 2f indicate that the NDP-MnO_2 sample exhibits a distinct crystal structure compared to pure NDP and MnO_2, confirming the successful synthesis of the composite material. This observation aligns with the nanoparticle dimensions quantified through transmission electron microscopy (TEM) characterization. Notably, the particle diameter measurements presented in Fig. 2c and the corresponding size distribution histograms in Figure S3 (Supporting Information) exhibit congruent morphological characteristics, collectively confirming the uniformity of the nanostructured system.

A further investigation into the thermal sensitivity of the NDP@MnO_2 hybrid hydrogel was conducted. As shown in Fig. 2e, when the NDP@MnO_2 hydrogel was placed in 37°C warm water, a sol-gel transition was observed. Rheological measurements were performed to further evaluate this thermal sensitivity (Fig. 2h). During the heating process, the storage modulus (G') and loss modulus (G") curves indicated that the sol-gel transition initiated at 26–30°C, suggesting that the transition is sensitive to body temperature. These results confirm the successful preparation of a bio-applicable, thermally responsive hybrid hydrogel. Hybrid hydrogels must possess sufficient adhesion ability in wet environments to meet the requirements for firmly fixing to moist wounds. Relevant literature has reported similar requirements for hydrogels in analogous application scenarios[34,35]. As shown in Fig. 2j, two pieces of porcine skin could be firmly adhered by the NDP dopamine group, demonstrating the hydrogel's reliable adhesiveness. When subjected to a 1 kg load, no relaxation was detected at the porcine skin joint, indicating strong tissue-adhesion properties. To simulate the moist environment of the abdominal cavity, the pancreatic wound adhered with the hydrogel was stirred in 36°C normal saline for 5 minutes to mimic postoperative conditions. As shown in Fig. 2k, the hydrogel remained tightly adhered to the pancreas after stirring, exhibiting no signs of swelling, dissolution, or detachment during agitation. This indicates its excellent adhesion properties in a wet environment. Stress-strain tests were conducted to evaluate the mechanical properties and fatigue resistance of the hydrogel (Fig. 2i). The results showed that the hydrogel exhibited robust mechanical strength, maintaining its integrity even under a tensile force of approximately 125 kPa. These findings demonstrate that NDP@MnO_2 possesses reliable adhesion and excellent mechanical properties in humid environments, meeting the practical requirements for treating pancreatic edema following wound deformation. As illustrated in Figure S5, after 20 days of dialysis with the NDP@MnO_2 hydrogel, the weight of NDP decreased by approximately 50%, whereas no substantial loss of MnO_2 nanoparticles was detected. These findings indicate the safety of locally applying the hydrogel. Collectively, these characteristics are essential for its potential application in pancreatic cancer treatment, as they ensure a stable presence at the surgical site and consistent efficacy throughout the treatment process.

Photothermal properties and in vitro experiments of hydrogels

Effectively eliminating locally residual tumor tissues using a hydrogel combined with photothermal therapy (PTT) after tumor resection is crucial for preventing pancreatic cancer recurrence[36,37]. As presented in Fig. 3a and b, In vitro photothermal properties of NDP@MnO_2 hydrogels embedded with different concentrations of MnO_2 nanoparticles were evaluated under 808 nm laser irradiation. The spatiotemporal temperature distribution and thermal variation curves within the irradiated regions were systematically analyzed to characterize their photothermal conversion behavior. Under 808 nm laser irradiation at a power density of 1.5 W/cm^2, the NDP@MnO_2 hydrogel containing 200 μg/mL MnO_2 nanoparticles exhibited excellent in vitro photothermal performance. The hydrogel demonstrated a rapid photothermal response, achieving a temperature increase of 50.0 °C ($\Delta T = 50.0$ °C) within 5 min. Such plasmonic-mediated heat generation constitutes the fundamental mechanism underlying the superior thermoresponsive behavior of NDP@MnO_2 hydrogels. When the temperature in the near-infrared (NIR)-irradiated region exceeded 45 °C, the hydrogel effectively induced tumor cell death while minimizing damage to non-exposed tissues, fulfilling the performance criteria for precise and efficient tumor tissue ablation[47]. Building on these findings, We conducted a thermal cycling experiment on the hydrogel and based on this, we measured the thermal efficiency of the hydrogel. The results are shown in Fig. 3c, d and e. Figure 3c represents a single thermal cycling experiment. The hydrogel was irradiated with an 808 nm near-infrared (NIR) laser at a power density of 1.5 W/cm^2 until the temperature reached approximately 50 °C, after which the laser was turned off to allow natural cooling to room temperature. The entire process was monitored using an infrared thermal imaging camera, and the temperature–time profile was recorded and plotted. The experimental results demonstrate that the NDP@MnO_2 hydrogel exhibits excellent photothermal conversion performance, confirming its performance for in vivo therapeutic applications. Figure 3d calculates the relationship between -lnθ and time based on the thermal cycling curve. Quantitative evaluation of the photothermal response revealed a high conversion efficiency of 45.7%. These findings unambiguously confirm

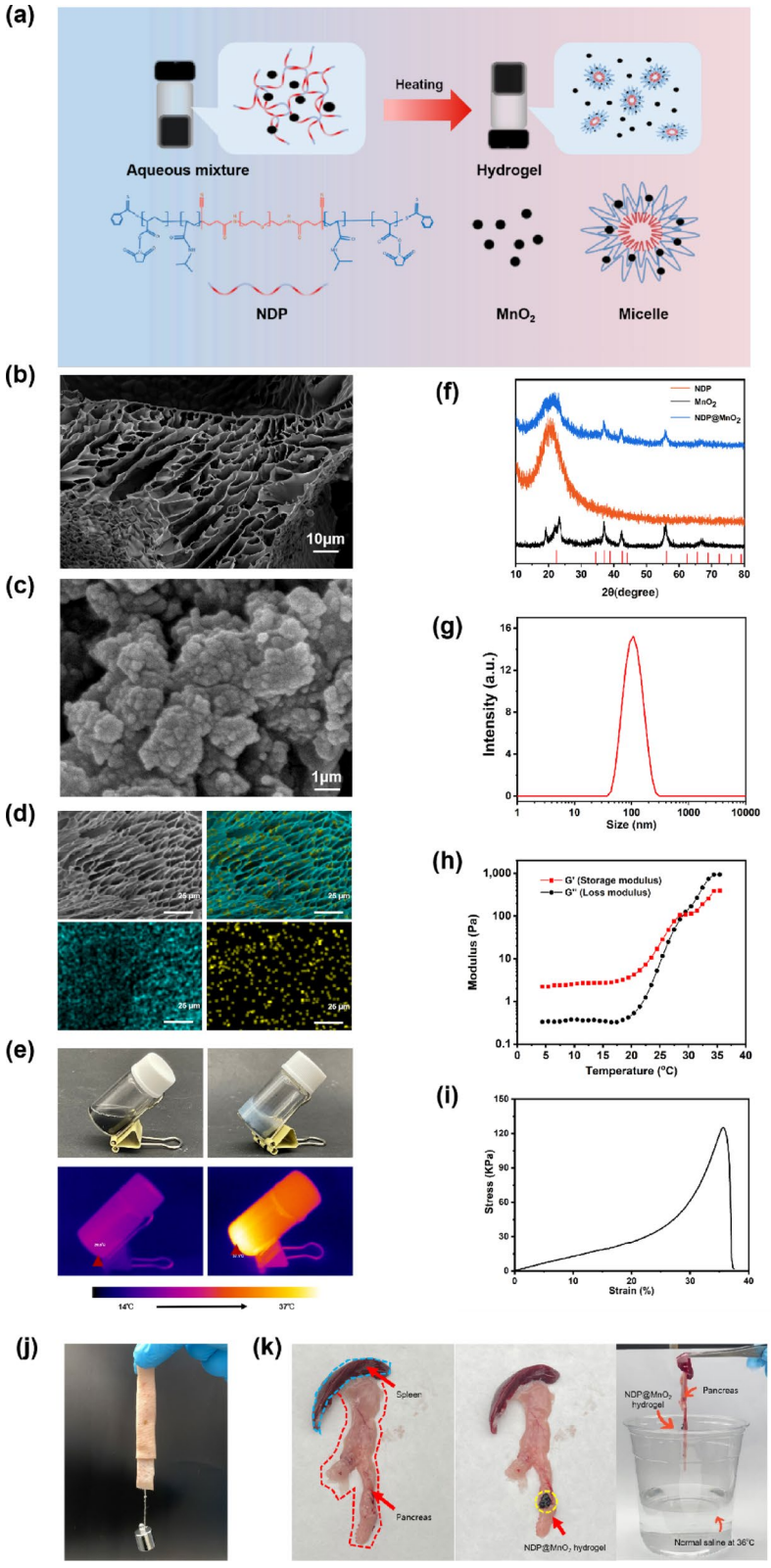

the well photothermal capability of our NDP@MnO_2 hybrid hydrogel system. Figure 3e conducts three thermal cycling experiments to verify the photothermal stability of the hydrogel. During the three thermal cycles, the NDP@MnO_2 hydrogel did not exhibit any decline in photothermal efficiency during the photothermal process. The results demonstrated that the hydrogel exhibited excellent thermal stability. The above experiments showed the photothermal efficiency and photothermal stability of the hydrogel and the results demonstrated its excellent photothermal performance.

PTT can significantly raise the local temperature of tumor tissue, accelerating the degeneration of tumor cell proteins and enhancing the action of drugs on tumor cells[38]. The high temperature inhibits the proliferation

◀**Fig. 2**. Characterization of the NDP@MnO_2 hydrogel. (**a**) Schematic illustration of the components constituting the NDP@MnO_2 hydrogel. (**b**) SEM image of NDP@MnO_2 Hydrogel. Scale bar, 10 μm. (**c**) SEM image of MnO_2 nanoparticles. Scale bar, 100 μm. (**d**) EDS mappings of C, O, and Mn elements in NDP@MnO_2 Hydrogel, respectively. Scale bar: 25 μm. (**e**) Digital images and corresponding infrared thermal images of NDP@MnO_2 Hydrogel under the heating process respectively. (**f**) XRD pattern of MnO_2, NDP and NDP@MnO_2 respectively. (**g**) DLS pattern of MnO_2. (**h**) Rheological measurements of G' and G" for the NDP@MnO_2 aqueous dispersion (NDP@MnO_2 hydrogel). (**i**) Tensile strength testing results for the NDP@MnO_2 hydrogel. (**j**) Digital images and evaluation of adhesion strength when the NDP@MnO_2 hydrogel is adhered to porcine skin. (**k**) Digital images and assessment of adhesion force in a pancreatic humid environment using NDP@MnO_2 hydrogel adhesive.

activity of tumor cells and promotes the exposure of antigen targets on apoptotic tumor cells[39]. The tumor antigen induces autologous anti-tumor immunity, generating a significant anti-tumor effect[40]. In recent years, Mn^{2+}, as an effective antitumor drug and immunoagonist, has been a research focus[41]. Mn^{2+} can inhibit tumor growth in a concentration dependent manner[42]. Mouse pancreatic cancer Panc-02 cells were selected to further evaluate the impact of the NPs content in the NDP@MnO_2 hydrogel on tumor growth. As shown in Fig. 3g, with the increase of MnO_2 NPs concentration, the inhibitory effect on the proliferation of Panc-02 cells became more obvious. The 24-hour survival rate of PBS group was 97.3%±1.2% while the survival rate of Panc-02 cells cultured with 200 mg/ml group for 24 h was only 15.6%±0.5%. The results showed that NDP@MnO_2 hydrogel could effectively inhibit the proliferation of Panc-02 cells. Furthermore, we do not know whether the use of photothermal therapy will enhance the killing effect of Panc-02 cells. Therefore, To further explore the efficacy of the NDP@MnO_2 hydrogel combined with PTT, in vitro experiments were conducted using mouse pancreatic cancer Panc-02 cells. We evaluated the in vitro cytotoxicity effect of hydrogels on cells under photothermal therapy by using Calcein-AM/PI stained cells. The dye caused dead cells to fluoresce red and living cells to fluoresce green. The killing effect of NDP@MnO_2 combined with 808 nm laser on Panc-02 cells was shown in Fig. 3f. As shown in Fig. 3h and i, cell counting and quantitative fluorescence analysis were conducted on digital images. No significant cell death was observed in either the PBS + PTT group or the PBS group. These results showed that 808 nm laser irradiation cannot be effective in killing tumor cells. In contrast, in the NDP@MnO_2 group, both the red fluorescence and the fluorescence absorbance of dead cells had significantly increased. Meanwhile, the cell survival rate decreased to 58%±1.4%. These results showed that Mn^{2+} could effectively induce apoptosis of tumor cells. There was almost no green fluorescence in the NDP@MnO_2 + PTT group, the absorbance of living cells was only 1.22 ± 0.06 and the survival rate was only 1%±0.2%. This showed that the photothermal effect induced by the 808 nm laser killed almost all tumor cells. The above results indicated that NDP@MnO_2 hydrogel combined with 808 nm laser synergistic therapy has remarkable destructive effects on tumor cells.

In vivo therapy of subcutaneous tumors in mice

The in vivo anti-tumor efficacy of the NDP@MnO_2 hydrogel in combination with 808 nm laser was evaluated using tumor-bearing C57BL/6J mice (Fig. 4a). The hyperthermic response within the tumor region was monitored using an infrared thermometer. Upon exposure to the 808 nm laser, the temperature at the tumor site in the NDP@MnO_2 hydrogel group was raised to approximately 50.9 °C within 5 min (Fig. 4b and e). This hyperthermia effect has been previously reported to be sufficient for inducing tumor cell apoptotic necrosis[43]. In contrast to the continuous tumor progression observed in other groups, the NDP@MnO_2 + PTT group exhibited no evidence of tumor recurrence after 14 days of treatment, demonstrating a significantly lower tumor recurrence rate compared to the other groups (Fig. 4f) ($P < 0.05$). No obvious recurrence was noted at the resection site in the NDP@MnO_2 + PTT group (Fig. 4c). The combination therapy of NDP@MnO_2 and 808 nm laser also showed a significant inhibitory effect on tumor recurrence, as illustrated in Fig. 4d, g and h. As shown in Fig S4, the 16-day weight curves of mice validated the superior anti-relapse efficacy of PTT. Histological analysis via H&E staining of tumor sections revealed evident apoptosis in the NDP@MnO_2 group, while no obvious tumor cells were detected in the NDP@MnO_2 + PTT group (Fig. 4i). Previous studies have reported that Mn^{2+} can effectively induce tumor cell apoptosis and promote effective anti-tumor immunity[44]. The hyperthermia pfurther enhances the expression of tumor antigens which together with Mn^{2+}, effectively activates the anti-tumor immune response, leading to the elimination of residual tumors[45,46]. As shown in Fig. 4j, The administration of MnO_2 nanoparticles activated anti-tumor immunity in mice, concurrently inducing glutathione (GSH) depletion and promoting downstream GPX4 expression. High GSH levels in tumor cells are known to attenuate the efficacy of reactive oxygen species (ROS)-based therapies, whereas GSH depletion potentiates the therapeutic benefits of thermotherapy[47]. The AOD statistical results of $CD4^+$, $CD8^+$ and GPX4 immunofluorescence positive signals further confirmed the effectiveness of the related anti-tumor immunity (Fig. 4k, l and m). Collectively, the integration of MnO_2-mediated photothermal ablation and hydrogel-mediated drug retention establishes NDP@MnO_2 as a promising platform for precision therapy in pancreatic cancer. By effectively addressing residual micrometastases, this strategy has the potential to redefine postoperative adjuvant treatment paradigms.

In situ treatment of rabbits PC by hydrogels

Due to the complex pathobiological characteristics of pancreatic cancer, constructing an in situ pancreatic cancer model is crucial for verifying the therapeutic efficacy of preventing postoperative recurrence[48]. As illustrated in Fig. 5a and b, an in-situ pancreatic cancer rabbit model was established to evaluate the anti-tumor recurrence effect of hydrogel in combination with laser therapy. Following anesthesia, the tumor was resected, and the

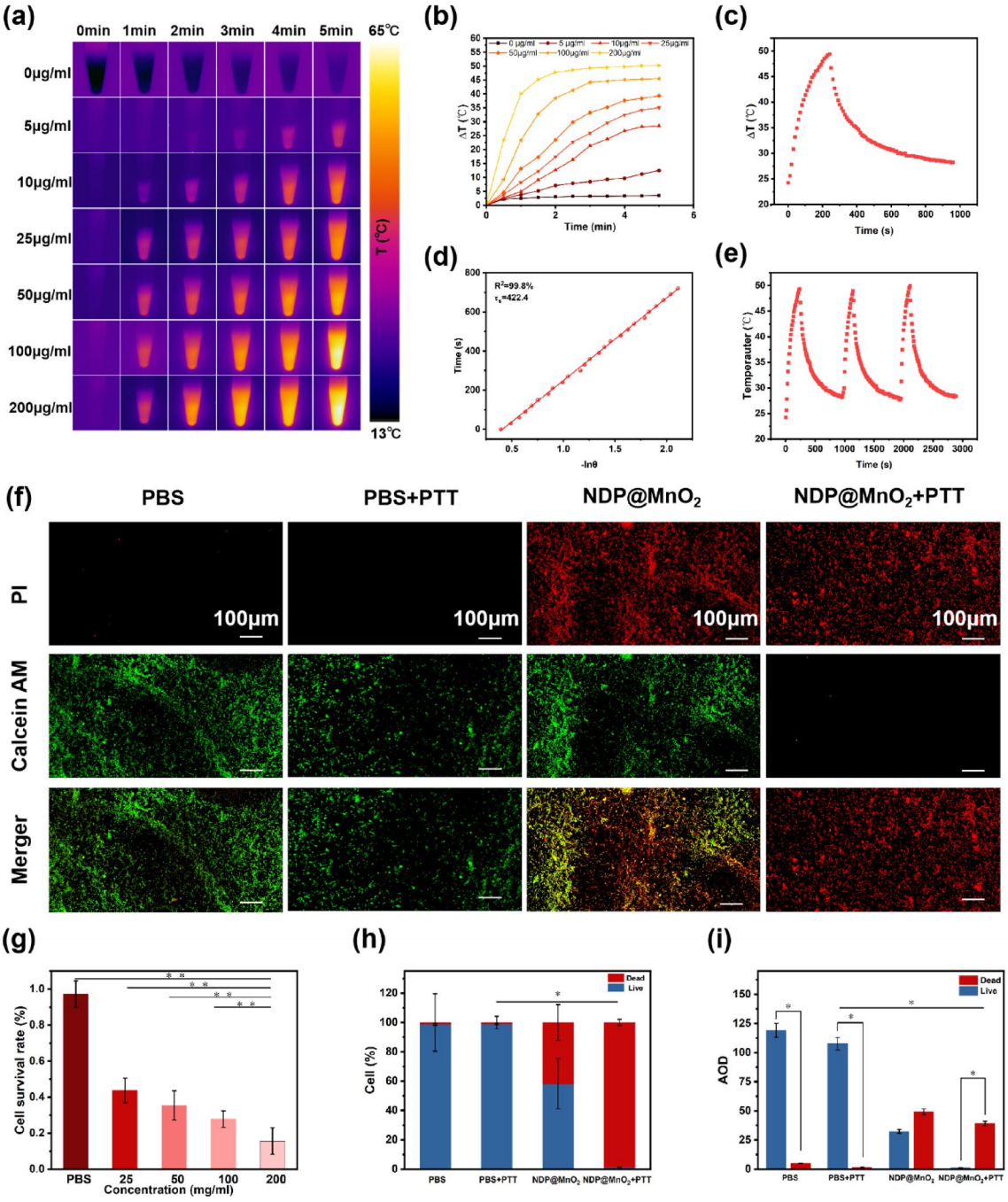

Fig. 3. In vitro photothermal andcytotoxic effects of NDP@MnO_2 hydrogel. (**a**) Infrared thermal images of NDP@MnO_2 hydrogel containing different concentrations of MnO_2 nanoparticles were captured respectively under the irradiation of 808 nm laser in vitro. (**b**)The temperature rising efficacy with various concentration of MnO_2 nanoparticles of NDP@MnO_2 hydrogel in vitro. (**c**) Photothermal performance of the aqueous dispersion of NDP@MnO_2 hydrogel under NIR irradiation by 808 nm laser at a power intensity of 1.5 $W(cm^2)^{-1}$ for periods, with the laser cut off when the temperature tended to be stable. (**d**) Time constant for heat transfer calculated from the cooling period. (**e**) Heating curve of NDP@MnO_2 hydrogel dispersed in water for three cycles at a power intensity of 1.5 $W(cm^2)^{-1}$ under irradiation by 808 nm laser respectively. (**f**) Live and dead cells were stained using Calcin-AM/PI after the photothermal experiment. Green fluorescence indicates live cells, and red fluorescence indicates dead cells. Scale bar, 100 μm. (**g**) Inhibition of Panc-02 cells by NDP@MnO_2 hydrogel with different concentrations. (**h**) Quantitative analysis of cell proportions from the digital images in (**f**) was performed using ImageJ software. (**i**) Fluorescence intensity analysis of the average optical density (AOD) from the images in (**f**) was conducted using ImageJ software.

hydrogel was subsequently injected into the surgical wound via a syringe. The hydrogel-coated wound was then subjected to photothermal therapy using an 808 nm laser. As show in Fig S4, rabbits treated with NDP@MnO_2+PTT maintained significantly higher body weights than the two control groups at day 16, validating the therapeutic efficacy of this combination strategy. Postoperative treatment outcomes were assessed by computed tomography (CT) imaging, as shown in Fig. 5c. Samples were collected from euthanized animals after 16 days. It was observed that there was no significant tumor recurrence in the NDP@MnO_2 + PTT group. As shown in Fig. 5d, histological analysis via H&E staining and TUNEL assays was conducted. The PBS group exhibited tightly arranged tumor cells with large blue-stained nuclei in the H&E staining. In contrast, the NDP@MnO_2 group showed evidence of tumor necrosis around the injection site, characterized by morphologically compromised tumor cells with broken cell membranes and necrotic areas. TUNEL staining revealed distinct necrosis foci in specific regions. Compared to other groups, the H&E and TUNEL images of the NDP@MnO_2 + PTT group demonstrated the absence of residual pancreatic tumor cells. Fluorescence analysis further corroborated the therapeutic efficacy of the hydrogel combined with laser treatment (Figs. 5e).

In summary, these findings indicate that the approach of combining NDP@MnO_2 hydrogel implantation at the surgical site with 808 nm laser irradiation holds significant promise for preventing postoperative recurrence of pancreatic cancer. This method contrasts with earlier research on conventional and multidisciplinary therapies (such as chemotherapy, radiotherapy, and immunotherapy) aimed at preventing postoperative recurrence of in-situ pancreatic tumors. Our injectable photothermal hydrogel can rapidly and completely eradicate residual tumors following in-situ pancreatic cancer surgery.

Biocompatibility of hydrogels

To evaluate the cytotoxicity of the hydrogel, the immortalized human liver epithelial cell line (THLE-2) and human acute monocytic leukemia cell line (THP-1) were incubated with the hydrogel for 24 h followed by Calcein-AM/PI live/dead staining. This dual staining protocol discriminates viable cells via green fluorescence (Calcein-AM, esterase-active) and non-viable cells via red fluorescence (PI, membrane-permeant nucleic acid staining). As demonstrated in Fig. 6a, no hydrogel-induced cell apoptosis or necrosis was observed after 24-hour co-culture. Quantitative analysis of fluorescent images confirmed that the hydrogel exhibited no significant cytotoxicity toward both cell lines under the tested conditions.

To assess the blood compatibility of the hydrogel, rabbit red blood cells were incubated with deionized water, normal saline, PBS, NDP@MnO_2, MnO_2, and NDP respectively, as shown in Fig. 6b and c. Compared to the negative control group (normal saline group) and the positive control group (distilled water group), the hemolysis rate of the NDP@MnO_2 group was less than 5%, indicating it falls within a safe range. Therefore, NDP@MnO_2 can be considered as a biocompatible material with favorable blood compatibility.

To further evaluate the in vivo biocompatibility of the hydrogel, the hydrogel was injected subcutaneously into the right hind leg of mice. After 14 days, major organs (heart, liver, spleen, lung, and kidney) and blood samples were collected. As shown in Fig. 6d, Histological examination using H&E staining revealed no evident signs of organ necrosis, inflammation, or ischemia. Figure 6e showed the blood biochemistry results. Compared with PBS group, there were no significant differences in biochemical indices such as creatinine (CREA), blood urea nitrogen (BUN), uric acid (UA), albumin (ALB), alanine aminotransferase (ALT), alkaline phosphatase (ALP), aspartate aminotransferase (AST), and total bilirubin (TBIL) in the NDP@MnO_2 group (P>0.05). Both groups exhibited normal levels of these indicators. Therefore, These findings collectively indicate that the NDP@MnO_2 hydrogel exhibits superior in vivo biocompatibility.

Conclusions

In summary, we have developed an innovative injectable thermosensitive NDP@MnO_2 hydrogel for adjuvant therapy in postoperative pancreatic cancer. This hydrogel combines excellent biocompatibility, tissue adhesion, photothermal properties, and anti-tumor capabilities. In vitro, its favorable cytocompatibility and controlled release of MnO_2 nanoparticles underpin its therapeutic functions. In vivo, when applied to the resection margins following pancreatic surgery, it adheres to the stump, seals the incision, and reduces the risk of complications. Notably, in combination with photothermal therapy, it significantly curbs cancer recurrence in both mouse and rabbit models by selectively eliminating residual tumor cells via localized hyperthermia while sparing adjacent healthy tissues. Distinct from traditional adjuvant therapies, this NDP@MnO_2 hydrogel-based approach enables spatially confined photothermal ablation, synergizes with surgical resection to prevent cancer cell dissemination, and targets residual microtumors, presenting a new paradigm for precision post-surgical intervention. However, the potential immune-related effects arising from the complex interactions among the hydrogel, MnO_2 nanoparticles, and immune cells in the tumor microenvironment require further investigation. For clinical translation, future research should focus on evaluating the efficacy and safety of this treatment strategy in large-animal models to determine optimal treatment parameters and generate reliable data for clinical applications. Overall, this novel hydrogel-based method holds significant promise for improving the prognosis of pancreatic cancer patients, potentially reducing recurrence rates and mortality.

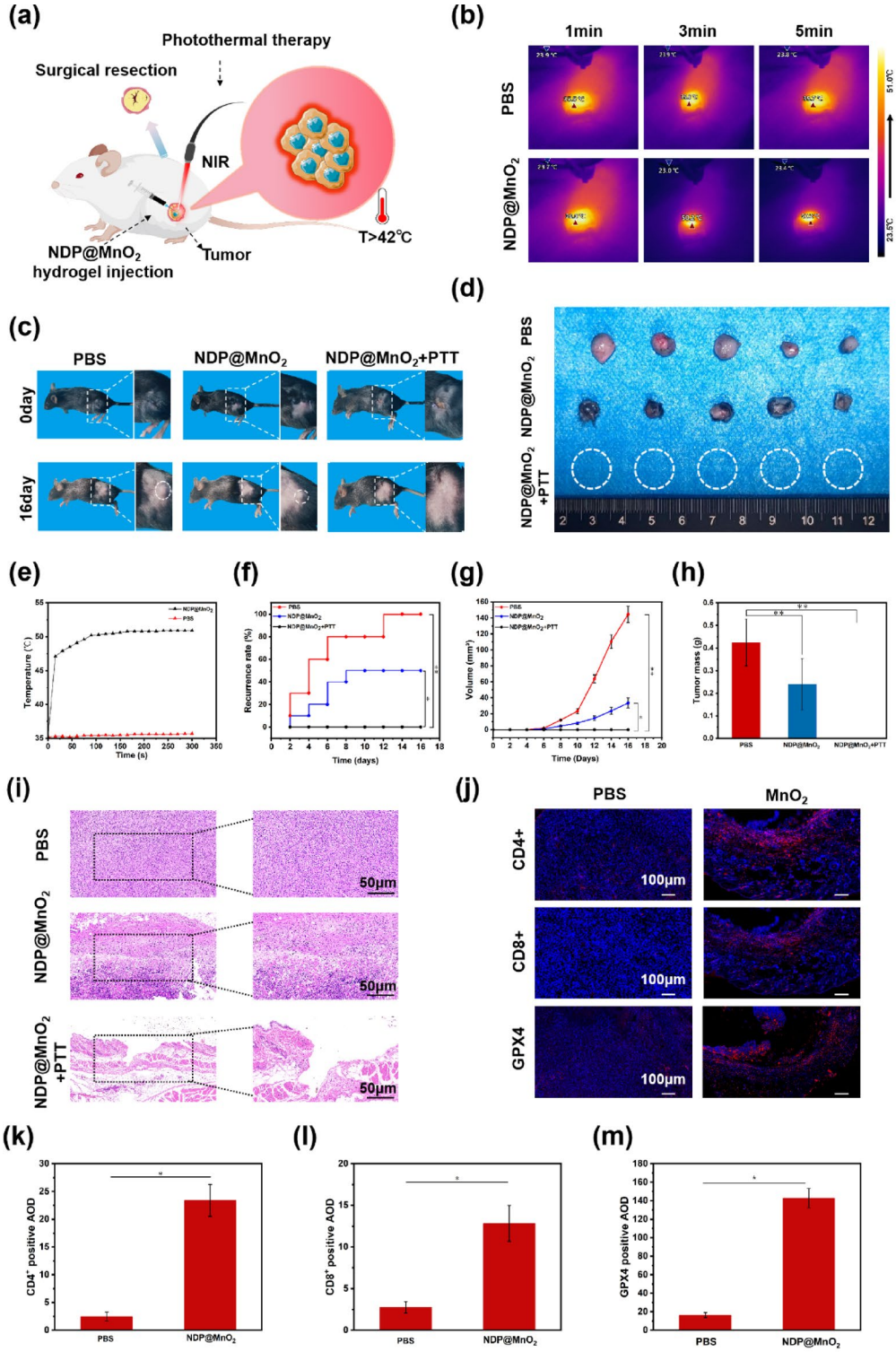
(a)
Photothermal therapy
Surgical resection
NIR
T>42℃
NDP@MnO2
hydrogel injection
Tumor
(b)
1min
3min
5min
PBS
NDP@MnO2
(c)
PBS
NDP@MnO2
NDP@MnO2+PTT
0day
16day
(d)
PBS
NDP@MnO2
NDP@MnO2 +PTT
(e)
Temperature (℃)
Time (s)
(f)
Recurrence rate (%)
Time (days)
(g)
Volume (mm3)
Time (Days)
(h)
Tumor mass (g)
(i)
PBS
NDP@MnO2
NDP@MnO2 +PTT
50μm
(j)
PBS
MnO2
CD4+
CD8+
GPX4
100μm
(k)
CD4+ positive AOD
(l)
CD8+ positive AOD
(m)
GPX4 positive AOD

◀**Fig. 4**. In vivo treatment of tumor bearing C57BL/6J mice. (**a**) Schematic diagram of the experimental design for tumor bearing mouse model. (**b**) Temperature changes in mice treated with PBS and NDP@MnO_2 hydrogel after exposure to an 808 nm laser for 5 min. (**c**) Photographs of postoperative mice from various treatment groups on day 0 (circles indicating tumor resection) and day 16 (circles indicating tumor recurrence). (**d**) Digital images of tumor tissues collected from various groups on day 16. Groups included: PBS (with no NDP@MnO_2 hydrogel and PTT), NDP@MnO_2 hydrogel (with no PTT), NDP@MnO_2 (with NDP@MnO_2 hydrogel and PTT). All tumor volumes were below the minimum detectable volume (5 mm^3) and are indicated by dashed circles. (**e**) The temperature rise curves of PBS and NDP@MnO_2 Hydrogel in mice after being exposed to 808 nm laser for 5 min respectively. (**f**) Tumor recurrence rates in different groups over 16 days. (**g**) The tumor tissues volume of various groups. Groups included: PBS (with no NDP@MnO_2 hydrogel and laser), NDP@MnO_2 hydrogel (with no laser), NDP@MnO_2 (with NDP@MnO_2 hydrogel and laser). Data are presented as mean ± S.D. ($n = 10$). *$P < 0.05$; **$P < 0.01$; ***$P < 0.001$. (**h**) Tumor average weights in different groups after 16 days. Data are presented as mean ± S.D. ($n = 10$). *$P < 0.05$; **$P < 0.01$; ***$P < 0.001$. (**i**) Ex vivo histological analysis of tumor sections after H&E staining (16 days post-treatment). Representative microphotographs of tumors tissue sections. Scale bar, 50 μm. (**j**) Representative microscopic images of immunohistochemistry of subcutaneous tumor tissues. (**k–m**) Quantitative analysis of the average optical density (AOD) of $CD4^+$, $CD8^+$, and GPX4 immunofluorescence-positive signals from the digital images in (**f**) was performed using ImageJ software. Data are presented as mean ± standard deviation (SD) with $n = 3$ biological replicates. Statistical significance was determined via Student's t-test, with significance levels denoted as *$P < 0.05$, **$P < 0.01$, and ***$P < 0.001$.

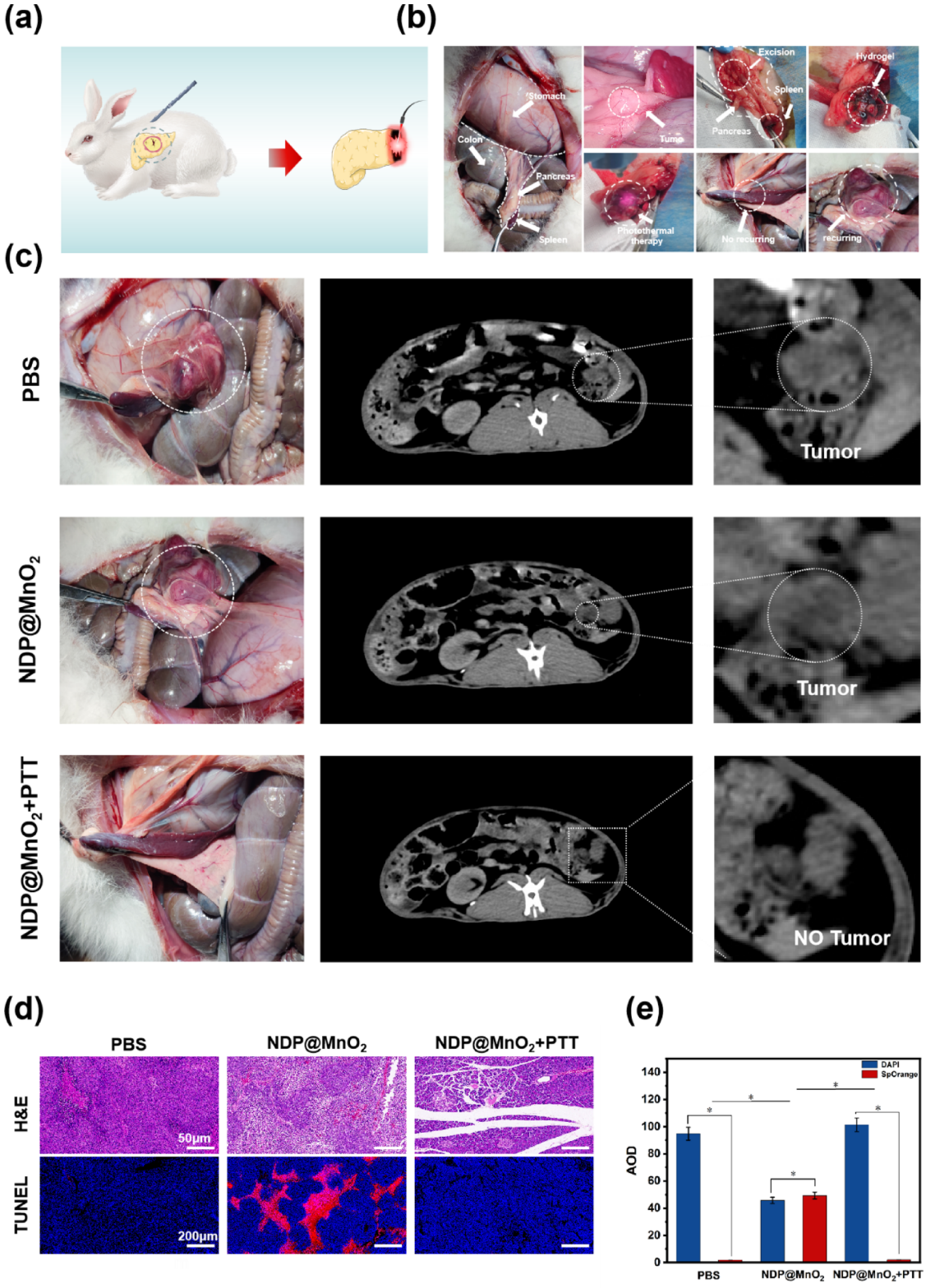
(a)
(b)
Stomach
Colon
Pancreas
Spleen
Tumor
Excision
Spleen
Pancreas
Hydrogel
Photothermal therapy
No recurring
recurring
(c)
PBS
NDP@MnO2
NDP@MnO2+PTT
Tumor
Tumor
NO Tumor
(d)
PBS
NDP@MnO2
NDP@MnO2+PTT
H&E
TUNEL
50μm
200μm
(e)
DAPI
SpOrange
AOD
0
20
40
60
80
100
120
140
PBS
NDP@MnO2
NDP@MnO2+PTT

◀**Fig. 5**. Evaluation of the Tumor-Suppressing Ability of NDP@MnO_2 Hydrogel with 808 nm Laser in Orthotopic Pancreatic Tumor-Bearing Rabbits. (**a**) Schematic diagram of the experimental design for orthotopic pancreatic cancer-bearing rabbits. (**b**) Digital images illustrating the process of using NDP@MnO_2 hydrogel combined with 808 nm laser treatment after in situ resection of pancreatic tumors in rabbits. (**c**) Intraoperative photographs obtained via laparotomy 16 days post-treatment, showing the presence or absence of recurrent pancreatic cancer (PC). CT coronal sections were analyzed to evaluate tumor recurrence, and specimens were collected for further examination. White circles indicate recurrent tumors. (**d**) Ex vivo histological analysis of tumor sections stained with H&E and TUNEL staining ($n = 3$). H&E Scale bar: 50 μm; TUNEL Scale bar, 200 μm. (**e**) Quantitative statistics of AOD of TUNEL fluorescence in each group were conducted using the ImageJ software. Data are expressed as mean ± S.D. ($n = 3$). $^{*}P<0.05$, $^{**}P<0.01$, $^{***}P<0.001$ by Student's t-test.

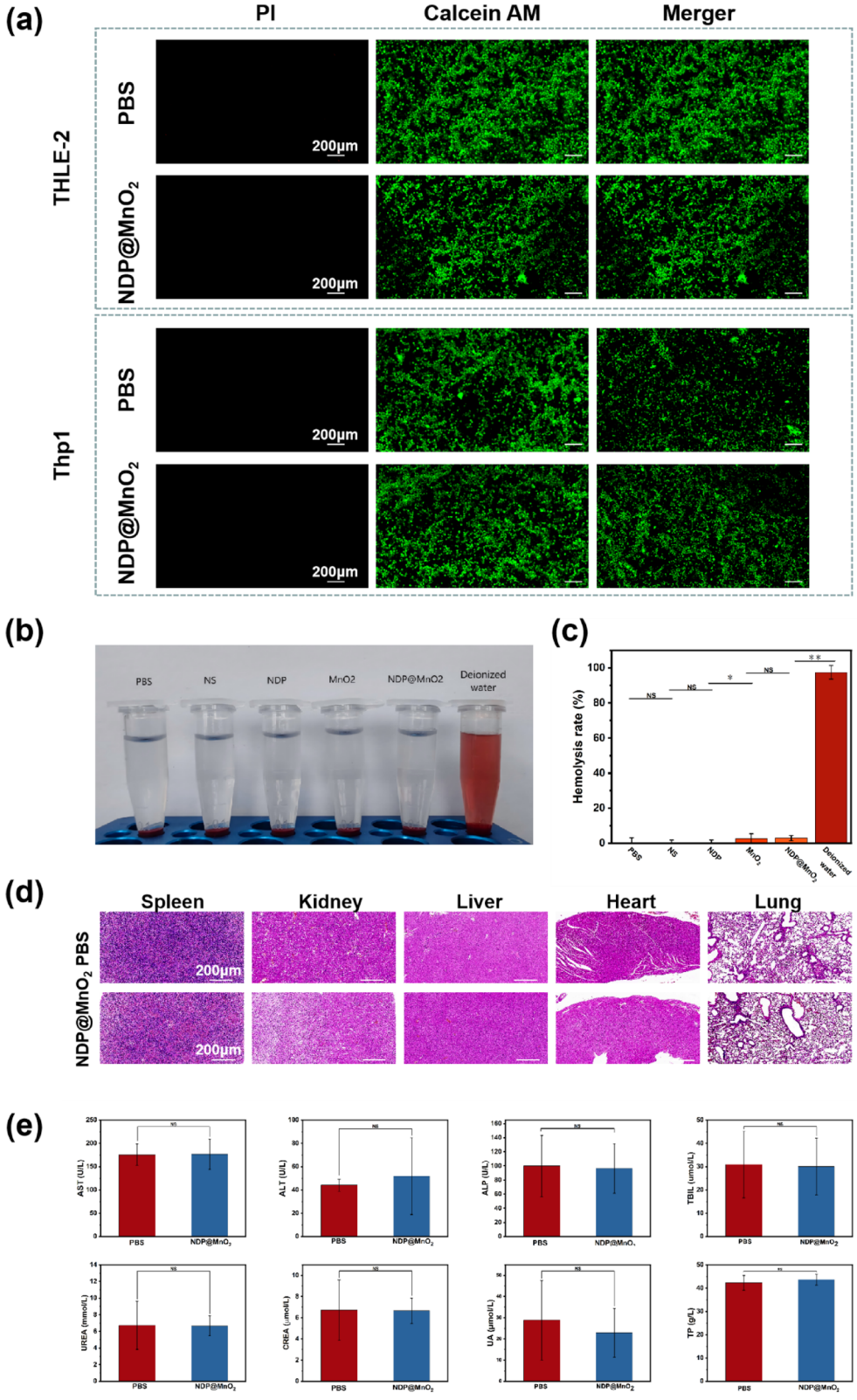
(a)
PI
Calcein AM
Merger
THLE-2
PBS
NDP@MnO2
Thp1
PBS
NDP@MnO2
200μm
(b)
PBS
NS
NDP
MnO2
NDP@MnO2
Deionized water
(c)
Hemolysis rate (%)
NS
*
**
(d)
Spleen
Kidney
Liver
Heart
Lung
NDP@MnO2 PBS
200μm
(e)
AST (U/L)
ALT (U/L)
ALP (U/L)
TBIL (umol/L)
UREA (mmol/L)
CREA (μmol/L)
UA (μmol/L)
TP (g/L)
PBS
NDP@MnO2

◀**Fig. 6**. Biological safety assessment of NDP@MnO_2 hydrogel. (**a**) The cytotoxicity was verified by co-culturing the cells with THLE-2 cells and THP1 cells with hydrogel. The results showed that NDP@MnO_2 had no obvious cytotoxicity to the cells. (**b**) Hemolysis rates of various components (distilled water, normal saline, PBS, NDP@MnO_2, MnO_2, and NDP) were evaluated using rabbit red blood cells. (**c**) Hemocompatibility analysis. NS (No Significance), **P*<0.05, ***P*<0.01 and ****P*<0.001. The hemolysis rate of NDP@MnO_2 was lower than 5%, indicating when the NDP@MnO_2 hydrogel was exposed to rabbit red blood cells, the hemolytic activity of NDP@MnO_2 was within the safe range. (**d**) Representative histological images of major organs (H&E staining) of mice in response to different treatments at day 14. ($n = 10$). Scale bar, 200 μm. (**e**) Serum biochemical and whole blood routine analyses of mice after implantation of the NDP@MnO_2 hydrogel and the treated with PBS rats serving as control ($n = 10$). Furthermore, all major serum biochemistry and critical hematological indices in each group remained within the normal range, indicating that the NDP@MnO_2 hydrogel did not cause any significant adverse effects.

Data availability

All data supporting the findings will be made publicly available upon request. Interested parties may contact the corresponding author, Zhengguang Wang, or the first author, Zhongxu Yuan, for access.

Received: 12 March 2025; Accepted: 20 June 2025
Published online: 02 July 2025

References

1. Strickler, J. H. et al. Sotorasib in KRAS p.G12C-Mutated advanced pancreatic Cancer. *N Engl. J. Med.* **388**, 33–43 (2023).
2. Klein, A. P. Pancreatic cancer epidemiology: Understanding the role of lifestyle and inherited risk factors. *Nat. Rev. Gastroenterol. Hepatol.* **18**, 493–502 (2021).
3. Ghaneh, P. et al. Immediate surgery compared with short-course neoadjuvant gemcitabine plus capecitabine, FOLFIRINOX, or chemoradiotherapy in patients with borderline resectable pancreatic cancer (ESPAC5): a four-arm, multicentre, randomised, phase 2 trial. *Lancet Gastroenterol. Hepatol.* **8**, 157–168 (2023).
4. van 't Land, F. R. et al. Dendritic Cell-Based immunotherapy in patients with resected pancreatic Cancer. *J. Clin. Oncol.* **42**, 3083–3093 (2024).
5. Schneider, M., Hackert, T., Strobel, O. & Büchler, M. W. Technical advances in surgery for pancreatic cancer. *Br. J. Surg.* **108**, 777–785 (2021).
6. De Dosso, S. et al. Treatment landscape of metastatic pancreatic cancer. *Cancer Treat. Rev.* **96**, 102180 (2021).
7. Seufferlein, T. et al. Perioperative or only adjuvant gemcitabine plus nab-paclitaxel for resectable pancreatic cancer (NEONAX)-a randomized phase II trial of the AIO pancreatic cancer group. *Ann. Oncol.* **34**, 91–100 (2023).
8. Labori, K. J. et al. Neoadjuvant FOLFIRINOX versus upfront surgery for resectable pancreatic head cancer (NORPACT-1): a multicentre, randomised, phase 2 trial. *Lancet Gastroenterol. Hepatol.* **9**, 205–217 (2024).
9. Zhang, X. et al. Perioperative or postoperative adjuvant oxaliplatin with S-1 versus adjuvant oxaliplatin with capecitabine in patients with locally advanced gastric or gastro-oesophageal junction adenocarcinoma undergoing D2 gastrectomy (RESOLVE): final report of a randomised, open-label, phase 3 trial. *Lancet Oncol.* **26**, 312–319 (2025).
10. Mintziras, I. et al. Postoperative morbidity following pancreatic cancer surgery is significantly associated with worse overall patient survival; systematic review and meta-analysis. *Surg. Oncol.* **38**, 101573 (2021).
11. Lee, Y. S. et al. Intraoperative radiation therapy induces immune response activity after pancreatic surgery. *BMC Cancer*. **21**, 1097 (2021).
12. Conroy, T. et al. Five-Year outcomes of FOLFIRINOX vs gemcitabine as adjuvant therapy for pancreatic cancer: A randomized clinical trial. *JAMA Oncol.* **8**, 1571–1578 (2022).
13. Naidu, J. et al. Combined chemotherapy and endoscopic ultrasound-guided intratumoral 32P implantation for locally advanced pancreatic adenocarcinoma: a pilot study. *Endoscopy* **54**, 75–80 (2022).
14. Biffi, G. & Tuveson, D. A. Diversity and biology of Cancer-Associated fibroblasts. *Physiol. Rev.* **101**, 147–176 (2021).
15. Morris, E. C., Neelapu, S. S., Giavridis, T. & Sadelain, M. Cytokine release syndrome and associated neurotoxicity in cancer immunotherapy. *Nat. Rev. Immunol.* **22**, 85–96 (2022).
16. Pfister, C. et al. Randomized phase III trial of Dose-dense methotrexate, vinblastine, doxorubicin, and cisplatin, or gemcitabine and cisplatin as perioperative chemotherapy for patients with Muscle-invasive bladder cancer. Analysis of the GETUG/AFU V05 VESPER trial secondary endpoints: chemotherapy toxicity and pathological responses. *Eur. Urol.* **79**, 214–221 (2021).
17. Spigel, D. R. et al. Five-Year survival outcomes from the PACIFIC trial: durvalumab after chemoradiotherapy in stage III Non-Small-Cell lung Cancer. *J. Clin. Oncol.* **40**, 1301–1311 (2022).
18. Yang, M., Li, J., Gu, P. & Fan, X. The application of nanoparticles in cancer immunotherapy: targeting tumor microenvironment. *Bioact Mater.* **6**, 1973–1987 (2021).
19. Yang, G., Ji, J. & Liu, Z. Multifunctional MnO(2) nanoparticles for tumor microenvironment modulation and cancer therapy. *Wiley Interdiscip Rev. Nanomed. Nanobiotechnol.* **13**, e1720 (2021).
20. Ndongwe, T. et al. The use of nanomaterials as drug delivery systems and anticancer agents in the treatment of triple-negative breast cancer: an updated review (year 2005 to date). *Discov Nano*. **19**, 138 (2024).
21. Tang, Z., Zhao, P., Wang, H., Liu, Y. & Bu, W. Biomedicine Meets Fenton chemistry. *Chem. Rev.* **121**, 1981–2019 (2021).
22. Han, H. S. & Choi, K. Y. Advances in nanomaterial-mediated photothermal cancer therapies: toward clinical applications. *Biomedicines* **9** (2021).
23. Liu, Q., Wu, B., Li, M., Huang, Y. & Li, L. Heterostructures made of upconversion nanoparticles and Metal-Organic frameworks for biomedical applications. *Adv. Sci. (Weinh).* **9**, e2103911 (2022).
24. Tao, J. et al. Targeting hypoxic tumor microenvironment in pancreatic cancer. *J. Hematol. Oncol.* **14**, 14 (2021).
25. Tan, Z. et al. Hypoxia: a barricade to conquer the pancreatic cancer. *Cell. Mol. Life Sci.* **77**, 3077–3083 (2020).
26. Zhang, H. et al. Hypoxia induces immunosuppression, metastasis and drug resistance in pancreatic cancers. *Cancer Lett.* **571**, 216345 (2023).
27. Xiao, Y. et al. Injectable thermosensitive hydrogel-based drug delivery system for local cancer therapy. *Colloids Surf. B Biointerfaces*. **200**, 111581 (2021).
28. Bernhard, S. & Tibbitt, M. W. Supramolecular engineering of hydrogels for drug delivery. *Adv. Drug Deliv Rev.* **171**, 240–256 (2021).

29. Zheng, H. & Zuo, B. Functional silk fibroin hydrogels: preparation, properties and applications. *J. Mater. Chem. B*. **9**, 1238–1258 (2021).
30. Barrett-Catton, E., Ross, M. L. & Asuri, P. Multifunctional hydrogel nanocomposites for biomedical applications. *Polymers (Basel)* **13** (2021).
31. Shen, Z. et al. Tumor Microenvironment-triggered nanosystems as dual-relief tumor hypoxia immunomodulators for enhanced phototherapy. *Theranostics* **10**, 9132–9152 (2020).
32. Wang, Q. et al. Multifunctional MnO(2)/Ag(3)SbS(3) nanotheranostic agent for Single-Laser-Triggered tumor synergistic therapy in the NIR-II Biowindow. *ACS Appl. Mater. Interfaces*. **14**, 4980–4994 (2022).
33. Zhang, P. et al. Tumor microenvironment-responsive nanohybrid for hypoxia amelioration with photodynamic and near-infrared II photothermal combination therapy. *Acta Biomater.* **146**, 450–464 (2022).
34. Wang, Z. et al. Recent advances of injectable in situ-forming hydrogels for preventing postoperative tumor recurrence. *Drug Deliv*. **31**, 2400476 (2024).
35. Zhang, J. et al. Injectable Drug-Conjugated DNA hydrogel for local chemotherapy to prevent tumor recurrence. *ACS Appl. Mater. Interfaces*. **12**, 21441–21449 (2020).
36. Chen, X. et al. Injectable hydrogels for the sustained delivery of a HER2-targeted antibody for preventing local relapse of HER2 + breast cancer after breast-conserving surgery. *Theranostics* **9**, 6080–6098 (2019).
37. Song, M., Liu, C., Chen, S. & Zhang, W. Nanocarrier-Based drug delivery for melanoma therapeutics. *Int. J. Mol. Sci.* **22** (2021).
38. Jain, T. & Dudeja, V. The war against pancreatic cancer in 2020 - advances on all fronts. *Nat. Rev. Gastroenterol. Hepatol.* **18**, 99–100 (2021).
39. Kesharwani, P. et al. Gold nanoparticles and gold nanorods in the landscape of cancer therapy. *Mol. Cancer*. **22**, 98 (2023).
40. Cai, Z. et al. Personalized neoantigen vaccine prevents postoperative recurrence in hepatocellular carcinoma patients with vascular invasion. *Mol. Cancer*. **20**, 164 (2021).
41. Batinic-Haberle, I. et al. H(2)O(2)-driven anticancer activity of mn porphyrins and the underlying molecular pathways. *Oxid. Med. Cell Longev.* **2021**, 6653790 (2021).
42. Zhu, D., Zhu, X. H., Ren, S. Z., Lu, Y. D. & Zhu, H. L. Manganese dioxide (MnO(2)) based nanomaterials for cancer therapies and theranostics. *J. Drug Target.* **29**, 911–924 (2021).
43. Bastiancich, C., Da Silva, A. & Estève, M. A. Photothermal therapy for the treatment of glioblastoma: potential and preclinical challenges. *Front. Oncol.* **10**, 610356 (2020).
44. Liang, L. et al. Progress of nanomaterials based on manganese dioxide in the field of tumor diagnosis and therapy. *Int. J. Nanomed.* **19**, 8883–8900 (2024).
45. Liang, J. L., Luo, G. F., Chen, W. H. & Zhang, X. Z. Recent advances in engineered materials for Immunotherapy-Involved combination Cancer therapy. *Adv. Mater.* **33**, e2007630 (2021).
46. Zhang, Y. et al. Pd@Au bimetallic nanoplates decorated mesoporous MnO(2) for synergistic Nucleus-Targeted NIR-II photothermal and Hypoxia-Relieved photodynamic therapy. *Adv. Healthc. Mater.* **9**, e1901528 (2020).
47. Yuan, H. et al. Photothermal nanozymatic nanoparticles induce ferroptosis and apoptosis through tumor microenvironment manipulation for Cancer therapy. *Small* **18** (41), e2202161 (2022).
48. Heinrich, M. A., Mostafa, A., Morton, J. P., Hawinkels, L. & Prakash, J. Translating complexity and heterogeneity of pancreatic tumor: 3D in vitro to in vivo models. *Adv. Drug Deliv Rev.* **174**, 265–293 (2021).

Acknowledgements

The authors acknowledge the financial support from the Scientific Research Project of Anhui Provincial Healthcare Commission (AHWJ2022a003), the University Research Project of Anhui ProVince (2022AH052328) and the Graduate Research Innovation Project of Bengbu Medical University (Byycxz24047).

The authors also acknowledge the implementation of animal experiments and the writing of the article supports by Sun Tianci and Xu Yan from Hefei University of Technology.

Author contributions

Author Contributions StatementZX.Y. and ZG. W.: ConceptualizationZX.Y., M.X., S.M. and DQ.L: Methodology and ValidationZX.Y., S.M.: Conceptualization, InvestigationZX.Y., ZG.W. and S.M.: WritingZG. W., ZX.Y. and L.Y.: Resources and Funding AcquisitionDQ.L. and WC.W.: SupervisionS. M. and BW. H.: Software and Data AnalysisG. C.:Project AdministrationAll authors have read and agreed to the published version of the manuscript.The authors declare no conflict of interest.

Declarations

Competing interests

The authors declare no competing interests.

Additional information

Supplementary Information The online version contains supplementary material available at https://doi.org/10.1038/s41598-025-08431-2.

Correspondence and requests for materials should be addressed to Z.W.